



Sensitivity analysis of attenuation in convective rainfall at X-Band frequency using the Mountain Reference Technique

Guy Delrieu, Anil Kumar Khanal, Frédéric Cazenave, and Brice Boudevillain

5

HMCIS Team, Institute for Geosciences and Environmental research (IGE),
UMR 5001 (Université Grenoble Alpes, CNRS, IRD, Grenoble-INP), Grenoble, France

Abstract. The RadAlp experiment aims at improving quantitative precipitation estimation (QPE) in the Alps thanks to X-band polarimetric radars and *in-situ* measurements deployed in the region of Grenoble, France. In this article, we revisit the physics of propagation and attenuation of microwaves in rain. We first derive four attenuation – reflectivity (AZ) algorithms constrained or not by path-integrated attenuations (PIA) estimated from the decrease in return of selected mountain targets when it rains compared to their dry-weather levels (the so-called Mountain Reference Technique - MRT). We also consider one simple polarimetric algorithm based on the profile of the total differential phase shift between the radar and the mountain targets. The central idea of the work is to implement these five algorithms all together in the framework of a generalized sensitivity analysis in order to establish useful parameterizations for QPE. The parameter structure and the inherent mathematical ambiguity of the system of equations make it necessary to organize the optimization procedure in a nested way. The core of the procedure consists in (i) exploring with classical sampling techniques the space of the parameters allowed to be variable from one target to the other and from one time step to the next, (ii) computing a cost function (CF) quantifying the proximity of the simulated profiles and (iii) selecting parameters sets for which a given CF threshold is exceeded. This core is activated for series of values of parameters supposed to be fixed, e.g. the radar calibration error for a given event. The sensitivity analysis is performed for a set of three convective events using the 0° -elevation PPI measurements of the Météo-France weather radar located on top of the Moucherotte Mount (altitude of 1901 m asl). It allows estimation of critical parameters for radar QPE using radar data alone. In addition to the radar calibration error, this includes time series of radome attenuation and estimations of the coefficients of the power-law models relating the specific attenuation and the reflectivity ($A-Z$ relationship) on the one hand and the specific attenuation and the specific differential phase shift ($A-K_{dp}$ relationship) on the other hand. It is noteworthy that the $A-Z$ and $A-K_{dp}$ relationships obtained are consistent with those derived from concomitant drop size distribution measurements at ground level, in particular with a slightly non-linear $A-K_{dp}$ relationship ($A = 0.275 K_{dp}^{1.1}$). X-Band radome attenuations as high as 15 dB were estimated, leading to the recommendation of avoiding the use of radomes for remote sensing of precipitation at such frequency.

Correspondence to: guy.delrieu@univ-grenoble-alpes.fr



1. Introduction

Estimation of atmospheric precipitation is important in a high mountain region such as the Alps for the assessment and management of water and snow resources (drinking water, hydro-power production, agriculture and tourism) as well as for prediction of natural hazards associated with intense precipitation and snowpack melting. In complement with *in-situ* raingauge networks and snowpack monitoring systems, remote sensing using ground-based weather radar systems has a high potential that needs to be exploited but also a number of limitations that need to be surpassed. A first dilemma is related to the choice of the altitude of the radar setup with a compromise to be found between maximizing the visibility of the radar system(s) at the regional scale and increasing the representativeness of the measurements made in altitude with respect to precipitation reaching the ground, especially during cold periods. A second dilemma is the well-known detection / resolution *versus* attenuation compromise, which is acute for weather radar frequencies. S-Band and C-Band frequencies (around 3 and 5 GHz, respectively) are traditionally preferred in continental-wide weather radar networks (Serafin and Wilson, 2000; Saxion et al. 2011, Saltikoff et al. 2019) for their appropriate precipitation detection capability and their moderate sensitivity to attenuation. In Europe, MeteoSwiss has the longest-standing experience in operating such a C-Band weather radar network in high-mountain regions (Joss and Lee, 1995; Germann et al. 2006; Sideris et al. 2014; Foresti et al. 2018). Implementation of radars operating at the X-Band frequency (~9-10 GHz) has also been proposed in the last decades for research and operational applications at local scales, e.g., for precipitation monitoring in urban areas and/or in mountainous regions (Delrieu et al. 1997; McLaughlin et al. 2009; Scipion et al. 2013; Lengfeld et al. 2014, to name just a few). The renewed interest for the X-Band frequency, known for long to be prone to attenuation (e.g., Hirschfeld and Bordan 1954), is based on the promises of polarimetric techniques (e.g. Bringi and Chandrasekar 2001; Ryzhkov et al. 2005) for attenuation correction (Testud et al. 2000; Matrosov and Clark, 2002; Matrosov et al. 2005; Matrosov et al. 2009; Koffi et al. 2014, Ryzhkov et al. 2014). Météo-France has chosen to complement the coverage of its operational radar network ARAMIS (for Application Radar à la Météorologie Infra-Synoptique) in the Alps by means of X-Band polarimetric radars. A first set of three radars was installed in Southern Alps within the RHytMME project (Risques Hydrométéorologiques en Territoires de Montagnes et Méditerranéens) in the period 2008-2013 (Westrelin et al. 2012; Yu et al. 2018). An additional radar (MOUC radar, hereinafter) was installed in 2014 on top of the Mount Moucherotte (1901 m) that dominates the valley of Grenoble. The RadAlp experiment (Khanal et al. 2019; Delrieu et al. 2020) is a contribution to research aimed at improving quantitative precipitation estimation (QPE) based on the Météo France MOUC radar, complemented by a suite of sensors installed on the Grenoble valley floor at the Institute for Geosciences and Environmental research (IGE, 210 m asl). This includes the IGE research X-Band polarimetric radar named XPORT, a K-Band Micro Rain Radar (MRR) and *in-situ* sensors (disdrometers, raingauges).

The present article aims to show that mountain returns can be useful for the parameterisation of QPE algorithms for weather radar systems operating at attenuating frequencies in mountainous regions. It is part of a series of contributions devoted to the Surface Reference Technique proposed for spaceborne radar configuration (Meneghini et al. 1983; Marzoug and Amayenc, 1994; and more recently Meneghini et al. 2020) and its transposition to ground-based radar configurations with the Mountain



65 Reference Technique (Delrieu et al. 1997, Serrar et al. 2000, Delrieu et al. 2020). Figures 1 and 2 illustrate our point. Figure 1 shows a map of dry-weather mountain returns of the MOUC radar. The configuration of the radars operated in the RadAlp experiment is recalled in the insert; note that only the MOUC radar data is used in the current study. The measurements are taken at an elevation angle of 0° which corresponds to the lowest PPI of the volume-scanning strategy of the MOUC radar. The reflectivity data are averaged over a period of four hours; one PPI is performed at the 0° -elevation angle every five minutes.

70 We have selected 22 mountain targets corresponding to compact groups of gates in successive radials (3-6 typically; the radial spacing is 0.5°) and ranges (5-10 gates; the gate extent is 240 m) presenting a majority of dry-weather reflectivity values greater than 45 dBZ. The paths between the radar and the targets are free of beam blockages and present as few noisy gates (due to side lobes) as possible. In addition to the reflectivity map, the top graphs of Fig.2 display the co-polar correlation (ρ_{hv}) and the total differential phase shift (Ψ_{dp}) maps at 14:00 UTC on 21 July 2017 before the convective event that occurred that

75 day between 15:30 and 18:00 UTC. The Ψ_{dp} map is essentially noisy at that time and the red colour in the ρ_{hv} map, corresponding to values close to 1, highlights some small rain cells, in particular one in the south of the radar domain close to Target 22 (Grand Veymont Mount). The middle row maps correspond to the occurrence of intense precipitation over the city of Grenoble at 16:05 UTC. A peak of 40 mm h^{-1} in ten minutes was recorded at that time by the raingauge located on top of the IGE building. The Ψ_{dp} map displays marked increasing radial profiles in the North-East (NE) direction. The ρ_{hv} map

80 allows a good delimitation of the whole rain pattern and clearly shows the dominance of the mountain returns over the rain returns for most of the Belledonne and Taillefer targets. The most striking observation on the reflectivity map is the dramatic decrease of the mountain returns of Targets 1-10 in the NE sector which results with no doubt from the rain cell falling over the city of Grenoble at that time. This is a clear example of what will be termed as “along-path attenuation” hereinafter. On the bottom row of Fig. 2, which corresponds to the measurements made at 17:00 UTC, one can observe a similar strong along-

85 path attenuation in the NE direction in the Ψ_{dp} map, associated with a second 40 mm h^{-1} rainrate peak at the IGE site (see eventually the hyetograph in Delrieu et al. (2020), their Fig. 2). But more impressive is the general decrease of returns from all the mountain targets, associated with a rain cell occurring at the radar site. This is an example of so-called “on-site attenuation”, related to the formation of a water film on the radome, combined with along-path attenuation in the immediate vicinity of the radar site.

90

The article is organised as follows. In the theoretical part (section 2), we find useful to revisit in some detail the physics of propagation and attenuation of microwaves in rain. We derive (section 2.2) four attenuation – reflectivity (AZ) algorithms constrained or not by path-integrated attenuations (PIA) estimated from the decrease in return of selected mountain targets when it rains, compared to their dry-weather levels. We also consider one simple polarimetric algorithm based on the profile

95 of the total differential phase shift between the radar and the mountain targets (section 2.3). The structure and interdependencies of the parameters are discussed in section 2.4. This leads to the description of the principles of the generalized sensitivity



analysis proposed for studying the physical model at hand (section 3.1). The results obtained are illustrated and discussed item by item in sub-sections 3.2.1-3.2.5. Concluding remarks and future work are presented in section 4.

2. Theory

100

2.1 Basic definitions and notations

Let us express the radar returned power profile $P(r)$ [mW] as:

$$P(r) = (C/r^2) Z(r) AF(r) \quad (2.1)$$

where $Z(r)$ [$\text{mm}^6 \text{m}^{-3}$] is the true reflectivity profile, $AF(r)$ [-] is the attenuation factor at range r [km] and C is the radar constant. We suppose the measured reflectivity profile $Z_m(r)$ to depend both on the attenuation and on a possible radar calibration error denoted dC :
105

$$Z_m(r) = P(r) r^2 / C = Z(r) AF(r) dC \quad (2.2)$$

In addition to the running range r , let us consider the range r_0 corresponding to the blind range of the radar system, eventually extended to the range where the reflectivity measurements start to be free of spurious detections due e.g. to side lobes.

110 The attenuation factor $AF(r)$ is expressed as the product of two terms:

$$AF(r) = AF(r_0) AF(r_0, r) \quad (2.3)$$

where $AF(r_0)$ is the on-site attenuation factor which, as discussed in the introduction, may result from two main sources: attenuation due to a water film on the radome and along-path attenuation due to precipitation falling between the radar site and range r_0 .

115 As a classical formulation (e.g. Marzoug and Amayenc, 1994), we express the two-way attenuation factor as a function of the specific attenuation profile $A(r)$ [dB km^{-1}] through the following equation:

$$AF(r) = AF(r_0) \exp(-0.46 \int_{r_0}^r A(s) ds) \quad (2.4)$$

To go further, we have to introduce relationships between the radar measurables (specific attenuation and reflectivity) and the variable of interest for QPE, i.e. the rainrate R [mm h^{-1}], which are assumed to be of power type with the following notations:

120 $A = a_{AZ} Z^{b_{AZ}}$ (2.5)

$$R = a_{RA} A^{b_{RA}} \quad (2.6)$$

$$R = a_{RZ} Z^{b_{RZ}} \quad (2.7)$$



The order used for the variables in equations 2.5-2.7 is meaningful since the specific attenuation profile is derived from the measured reflectivity profile, while the rainrate profile can be derived in a second step either from the specific attenuation
125 profile or from the corrected reflectivity profile. Due to the well-known lower variability of the R - A relationship compared to the R - Z relationship, (2.6) should be preferred to (2.7) for the estimation of the rainrate profiles (Ryzhkov et al. 2014).

Let us now consider another particular range, denoted r_m , where estimates of the attenuation factor may be available. We use the following notation:

$$130 \quad AF_m(r_m) = AF(r_m) dAF_m \quad (2.8)$$

where $AF(r_m)$ is the true attenuation factor at range r_m and the term dAF_m represents a multiplicative error term. As illustrated in the introduction, such direct estimates of the attenuation factor can be obtained in mountainous regions from the MRT.

135 We frequently use hereinafter the notion of path-integrated attenuation (PIA), in units of dB, defined as:

$$PIA(r) = -10 \log_{10}(AF(r)) \quad (2.9)$$

Note that since $AF(r)$ is comprised between 1 (no attenuation) and 0 (full attenuation), the PIA subsequently takes values in
140 the range of 0 (no attenuation) up to $+\infty$ (full attenuation). The PIAs at ranges r_0 and r_m are denoted PIA_0 and PIA_m , respectively, in the following.

2.2 Formulation of the attenuation-reflectivity algorithms

145 The following mathematical developments are inspired by the works on rain-profiling algorithms in satellite measurement configuration (e.g., Meneghini et al. 1983; Marzoug, Amayenc 1994). The attenuation-reflectivity algorithms (A - Z algorithms) proposed in this section rely on two basic equations. The first one is the analytical solution of (2.4) when the power-law model (2.5) is supposed to represent perfectly the A - Z relationship. By taking the derivative of $AF^{b_{AZ}}(r_0, r)$ with respect to range r , one obtains:

$$150 \quad d(AF^{b_{AZ}}(r_0, r))/dr = AF^{b_{AZ}}(r_0, r)(-0.46 a_{AZ} b_{AZ} Z(r)^{b_{AZ}}) \quad (2.10)$$

Substitution of the true reflectivity by the measured reflectivity through (2.2) and integration between r_0 and r yields:



$$155 \quad AF^{b_{AZ}}(r_0, r) = 1 - 0.46 a_{AZ} b_{AZ} SZ(r_0, r) / (AF(r_0) dC)^{b_{AZ}}$$

with:

$$SZ(r_0, r) = \int_{r_0}^r Z_m(s)^{b_{AZ}} ds. \quad (2.11)$$

160

The second equation is obtained by integrating (2.10) up to range r_m and by introducing the attenuation factor estimate available at this range, yielding:

$$(AF(r_m) / AF(r_0))^{b_{AZ}} + 0.46 a_{AZ} b_{AZ} SZ(r_0, r_m) / (AF(r_0) dC)^{b_{AZ}} = 1 \quad (2.12)$$

165

We develop in the next sub-section four formulations of attenuation corrections for a supposedly homogeneous precipitation type, i.e. we assume the a_{AZ} and b_{AZ} coefficients to be constant along the propagation path. Each formulation filters out one of the four parameters a_{AZ} , dC , $AF(r_0)$ and $AF(r_m)$. Note that due to the mathematical expression of the intervening equations there is no possibility to filter out the b_{AZ} parameter, which will be assumed to be constant, close to a value of 0.8 (Ryzkhov et al. 2014), and to present a low sensitivity in the system of equations.

2.2.1 AZhb algorithm (independent of PIA_m)

This formulation is based on (2.11) only. In other words, it does not make use of PIA_m . By combining (2.11), (2.2) and (2.3), one obtains a corrected reflectivity profile through the following equation:

175

$$Z_{AZhb}(r) = Z_m(r) / [(AF(r_0) dC)^{b_{AZ}} - 0.46 a_{AZ} b_{AZ} SZ(r_0, r)]^{1/b_{AZ}} \quad (2.13)$$

The specific attenuation profile follows from the use of the A-Z power-law model (2.5):

180

$$A_{AZhb}(r) = a_{AZ} Z_m^{b_{AZ}}(r) / [(AF(r_0) dC)^{b_{AZ}} - 0.46 a_{AZ} b_{AZ} SZ(r_0, r)] \quad (2.14)$$

This formulation is equivalent to the solution proposed early by Hitschfeld and Bordan (1954), hence the proposed name *AZhb*. It can be termed as a “forward algorithm” since only the measured reflectivities between range r_0 and the running range r are used for the correction at range r . The minus sign between the two terms of the denominator indicates that the denominator is not prevented to tend towards 0 when the *SZ* cumulative term increases. This solution is subsequently known to be unstable and highly sensitive to calibration error, to inadequate values of the A-Z relationship coefficients and to on-site attenuation.

185



2.2.2 AZC algorithm (independent of dC)

190

The attenuation constraint (2.11) is now used to express dC as:

$$dC = [0.46 a_{AZ} b_{AZ} SZ(r_0, r_m) / (AF(r_0)^{b_{AZ}} - AF(r_m)^{b_{AZ}})]^{1/b_{AZ}} \quad (2.15)$$

195 which is introduced in (2.11) to yield:

$$AF_{AZC}^{b_{AZ}}(r_0, r) = [AF(r_0)^{b_{AZ}} SZ(r, r_m) + AF(r_m)^{b_{AZ}} SZ(r_0, r)] / AF(r_0)^{b_{AZ}} SZ(r_0, r_m) \quad (2.16)$$

The corrected reflectivity profile is then derived from (2.2), (2.3), (2.15) and (2.16) to read as:

200

$$Z_{AZC}(r) = Z_m(r) [AF(r_0)^{b_{AZ}} - AF(r_m)^{b_{AZ}}]^{1/b_{AZ}} / \{0.46 a_{AZ} b_{AZ} [AF(r_0)^{b_{AZ}} SZ(r, r_m) + AF(r_m)^{b_{AZ}} SZ(r_0, r)]\}^{1/b_{AZ}} \quad (2.17)$$

Note that in the previous derivations, the expression of dC given by (2.15) is used two times, first in the expression of
 205 $AF_{AZC}^{b_{AZ}}(r_0, r)$ from (2.11) and then in the substitution of dC in (2.2).

The specific attenuation profile follows from the use of the A-Z relationship (2.5):

$$A_{AZC}(r) = Z_m(r)^{b_{AZ}} [AF(r_0)^{b_{AZ}} - AF(r_m)^{b_{AZ}}] / \{0.46 b_{AZ} [AF(r_0)^{b_{AZ}} SZ(r, r_m) + AF(r_m)^{b_{AZ}} SZ(r_0, r)]\} \quad (2.18)$$

210

In addition to their independence with respect to dC , it is interesting to note that both the attenuation factor profile and the specific attenuation profile provided by the AZC algorithm do not depend on the a_{AZ} parameter. This parameter is however present in the expression of the reflectivity profile.

215

2.2.3 AZ α algorithm (independent of a_{AZ})

The attenuation constraint (11) is now used to express a_{AZ} as:

$$220 \quad a_{AZ} = [dC^{b_{AZ}} (AF(r_0)^{b_{AZ}} - AF(r_m)^{b_{AZ}})] / [0.46 b_{AZ} SZ(r_0, r_m)] \quad (2.19)$$



which can be introduced in (2.11) to yield:

$$AF_{AZ\alpha}^{bAZ}(r_0, r) = [AF(r_0)^{bAZ}SZ(r, r_m) + AF(r_m)^{bAZ}SZ(r_0, r)] / AF(r_0)^{bAZ}SZ(r_0, r_m) \quad (2.20)$$

225

Equation 2.20 is actually identical to the $AF_{AZC}^{bAZ}(r_0, r)$ expression (2.16). From (2.20), (2.2) and (2.3), the resulting corrected reflectivity profile can be expressed as:

$$Z_{AZ\alpha}(r) = Z_m(r)SZ(r_0, r_m)^{1/bAZ} / \{dC [AF(r_0)^{bAZ}SZ(r, r_m) + AF(r_m)^{bAZ}SZ(r_0, r)]\}^{1/bAZ} \quad (2.21)$$

230

One can note that $Z_{AZ\alpha}(r)$ is different from $Z_{AZC}(r)$ and that it depends on dC .

Next, it can be verified by using (2.21), (2.5) and (2.19) (a second time, for the necessary substitution of a_{AZ}) that the $AZ\alpha$ specific attenuation profile is identical to the AZC specific attenuation profile given by (2.18) with:

235

$$A_{AZ\alpha}(r) = Z_m(r)^{bAZ} [AF(r_0)^{bAZ} - AF(r_m)^{bAZ}] / \{0.46 b_{AZ} [AF(r_0)^{bAZ}SZ(r, r_m) + AF(r_m)^{bAZ}SZ(r_0, r)]\} \quad (2.22)$$

We emphasize that both the attenuation factor and specific attenuation profiles provided by the AZC and $AZ\alpha$ algorithms are identical. Moreover they do not depend on the a_{AZ} and dC parameters. This is *a priori* a very interesting property of these algorithms. However, the reflectivity profiles provided by the two algorithms are different and, in particular, the reflectivity profile of the $AZ\alpha$ algorithm depends on dC while the reflectivity profile of the AZC algorithm depends on a_{AZ} .

245

2.2.4 AZ0 algorithm (independent of PIA_0)

The attenuation constraint (2.11) can finally be used to express $AF(r_0)^{bAZ}$ as:

$$AF(r_0)^{bAZ} = [0.46 a_{AZ} b_{AZ}SZ(r_0, r_m) + (AF_m(r_m) dC)^{bAZ}] / dC^{bAZ} \quad (2.23)$$

250 which can be introduced in (2.11) to yield:

$$AF_{AZ0}^{bAZ}(r_0, r) = \{0.46 a_{AZ} b_{AZ}SZ(r, r_m) + AF(r_m)^{bAZ} dC^{bAZ}\} / \{0.46 a_{AZ} b_{AZ}SZ(r_0, r_m) + (AF_m(r_m) dC)^{bAZ}\} \quad (2.24)$$



255 The resulting corrected reflectivity profile is:

$$Z_{AZ0}(r) = Z_m(r) / \{ 0.46 a_{AZ} b_{AZ} SZ(r, r_m) + (AF_m(r_m) dC)^{b_{AZ}} \}^{1/b_{AZ}} \quad (2.25)$$

And the specific attenuation profile:

260

$$A_{AZ0}(r) = a_{AZ} Z_m(r)^{b_{AZ}} / \{ 0.46 a_{AZ} b_{AZ} SZ(r, r_m) + (AF_m(r_m) dC)^{b_{AZ}} \} \quad (2.26)$$

The AZ0 algorithm has the simplest mathematical expressions among the three algorithms using the PIA constraint. It looks like a “backward algorithm” since the reflectivity and the specific attenuation profiles estimated at the running range r depend only on the measured reflectivities between ranges r_m and r , while the AZC and AZ α algorithms make use of the entire measured reflectivity profile between r_0 and r_m for the estimations at range r .

The + signs in the denominators of eq. 2.18, 2.19, 2.21, 2.22, 2.25 and 2.26 are indicators of the inherent stability of the three algorithms using the PIA constraint, unlike the AZhb algorithm.

270

2.3 Formulation of a simple polarimetric algorithm

In the present study, we are making a basic use of polarimetry with the derivation of a PIA profile, denoted $PIA_{\Phi_{dp}}(r)$, from the profile of the total differential phase shift on propagation, denoted $\Phi_{dp}(r_0, r)$ [°]:

275

$$\Phi_{dp}(r_0, r) = 2 \int_{r_0}^r K_{dp}(s) ds \quad (2.27)$$

where K_{dp} is the specific differential phase shift on propagation [° km⁻¹]. Assuming a power-law relationship between the specific attenuation and the specific differential phase shift on propagation, with:

280

$$A = a_{AK} K_{dp}^{b_{AK}} \quad (2.28)$$

and using Eqs 2.4 and 2.9 yields:

$$285 \quad PIA_{\Phi_{dp}}(r) = PIA_0 + 2 a_{AK} \int_{r_0}^r K_{dp}^{b_{AK}}(s) ds \quad (2.29)$$



This polarimetry-derived PIA profile can be related to the PIA profiles obtained by integrating the AZ specific attenuation profiles given by Eqs 2.14, 2.18 and 2.26 (equivalently, the $PIA_{\Phi_{dp}}(r)$ profile could be derived as a function of range and related to the AZ specific attenuation profiles).

290

2.4 Analysis of the parameters of the considered physical model

Equations 2.11, 2.12 and 2.29 form a system of equations with seven parameters (or unknowns), namely the coefficients of the $A-Z$ relationship (a_{AZ}, b_{AZ}), the coefficients of the $A - K_{dp}$ relationship (a_{AK}, b_{AK}), the radar calibration error (dC), the on-site attenuation (PIA_0) and the path-integrated attenuation at range r_m (PIA_m). Estimation of the rainrate profiles will require two additional parameters, e.g. the two parameters (a_{RA}, b_{RA}) of the $R-A$ relationship. The prefactors and exponents of the so-called $Z - A - K_{dp} - R$ relationships are mutually dependent since they are determined by the shape, density and size distributions of the hydrometeors and their electromagnetic properties, largely driven by their solid *versus* liquid composition. These coefficients may vary considerably from one precipitation type to another. In addition, even for a given precipitation type, the actual $Z - A - K_{dp} - R$ relationships present an inherent variability with respect to the power-law models, associated with the greater or lesser proximity of the particle size distribution (PSD) moments associated to each particular variable (e.g. the 6th order PSD moment for the reflectivity, the 3.67th order PSD moment for the rainrate). As an ultimate complexity, when for a given propagation path various types of hydrometeors are successively encountered (e.g. rain, melting precipitation, snow), it would be desirable to apply the appropriate coefficients for the different precipitation types... provided one is able to determine them. As a simplification in the present work, we will be considering a homogeneous precipitation type (convective rainfall). Because of the mathematical form of the equations at hand and the likely mutual dependence of the exponents and prefactors of the power-law models, we will assume the exponents of the $A-Z$ and the $A - K_{dp}$ relationships to be constant for all the considered events while the prefactors will be allowed to vary for each single target and time step. The question of the $R-A$ conversion is left aside in this study.

310

From a physical point of view, the parameters dC , PIA_0 and PIA_m are mutually independent and *a priori* independent of the coefficients of the $Z - A - K_{dp} - R$ power-law models. It seems reasonable, and this is done in the following simulations, to assume the radar calibration error to be constant for a given precipitation event. Regarding on-site attenuation, Frasier et al. (2013) made a synthesis of previous theoretical and empirical studies, and provided an empirical model based on the comparison of the measurements of two X-Band radar systems in the French Southern Alps, one equipped with a radome and the other one being radomeless. From this article, we have devised two sampling strategies for the parameter PIA_0 . The first sampling strategy is a simple random draw of PIA_0 between 0 and 10 dB whatever the precipitation conditions at the radar site. The second one takes into account a dependence of PIA_0 on the measured reflectivity in the vicinity of the radar site, denoted Z_0 . Based on Figure 5 in Frasier et al. (2013), we have fitted a coarse power-law model for X-band radome attenuation

315



320 on their experimental data, yielding $PIA_0^* = 0.0126 Z_0^{1.6}$ with PIA_0^* in dB and Z_0 in dBZ. Based on their Fig. 6 which shows
important variations between the theoretical and empirical results proposed in the literature, we have defined a large range of
lower and upper limits for the PIA_0 draws conditioned on Z_0 via PIA_0^* (see Table 1). For the two sampling strategies, PIA_0
will be allowed to vary from one target to the next, i.e. in different directions, and from one time step to the next. The accuracy
of the MRT-derived PIA_m was studied by Delrieu et al. (1999) by comparing MRT estimates with direct measurements
325 obtained with a receiving antenna set up in the mountain range. They showed that (i) selecting strong mountain returns
(typically greater than 45-50 dBZ) allows to mitigate the impact of precipitation falling over the target (negative bias), (ii) that
a refined estimation of the so-called dry-weather baseline is required to account for the possible modification of backscattering
properties of the mountain surfaces before and after the event and (iii) that the time variability of the dry-weather returns
defines the minimum detectable PIA. These elements were accounted for in the present study by selecting strong mountain
330 targets, studying their dry-weather time variability (see also Delrieu et al. 2020) and subsequently defining the range of
variation of the dAF_m multiplicative error (Table 1).

3. Sensitivity analysis

335 3.1. Principle

The parameter structure analyzed in sub-section 2.4 led us to organize the optimization procedure in a nested way:

For a series of convective events, we assume the exponents of the $A-Z$ and $A - K_{dp}$ relationships to be constant;

340 For each event, we assume the radar calibration error to be constant. A simulation is performed for each combination of the
 b_{AZ} , b_{AK} and dC values listed in Table 1;

The simulation core is implemented as follows for each mountain target and each time step:

- The $Z_m(r)$ and $\Phi_{dp}(r)$ profiles between the radar and the mountain target are pre-processed. For each of the
successive radials composing the target, this includes determination of gates affected by clutter in the region of the
345 mountain target and along the propagation path. This is done by considering both dry-weather mean values exceeding
various thresholds (25 dBZ for significant clutter, 45 dBZ for a gate belonging to the mountain target) and by using
the profile of the copolar correlation coefficient (ρ_{hv}) (Delrieu et al. 2020). The median $Z_m(r)$ and $\Phi_{dp}(r)$ profiles
over the series of radials are then computed. The MRT PIA_m is evaluated as the difference of the Z_m mean values
between the dry-weather baseline and the current time step, the mean being taken over all the gates composing the
350 target. The r_0 value is estimated as the range of the first gate for which four successive values (corresponding to a
range extent of 960 m) exceeds a ρ_{hv} value of 0.95. This last value is set as a threshold between precipitation and
clutter / no precipitation (from the statistics presented in Khanal et al. 2019). The Z_0 value is computed as the product



of $1/dC$ (correction for the radar calibration error) and the mean reflectivity of the selected four successive gates if they are located within the first 2 km range; otherwise the Z_0 value is set to 0. The reader is referred to Khanal et al. (2022) for the most recent description of the fairly sophisticated procedure used for the $\Phi_{dp}(r)$ regularization based on the raw total differential phase shift profiles for all the radials associated with a given target. Note that a target is selected at a given time step for the following steps of the simulation if $PIA_m > 1$ dB and if a good quality index of the $\Phi_{dp}(r)$ regularization is obtained (Khanal et al. 2022).

- The Latin Hypercubes Sampling technique is then used to generate N parameter sets (with $N = 200$ in the following) filling uniformly the parameter space composed of four parameters: the prefactors a_{AZ} and a_{AK} , the on-site attenuation factor $AF(r_0)$ and the multiplicative error dAF_m on the MRT attenuation factor. The central values and intervals of variation of these four parameters are listed in Table 1. It is noteworthy that the random draws are made on the dB-transformed ranges of parameters so that there are as many values below and above the central value, e.g. as many values between 0.15 and 0.3 on the one hand and between 0.3 and 0.6 on the other hand for the a_{AK} parameter.
- After discarding unphysical parameter sets (e.g. those leading to $PIA_0 > PIA_m$), the five algorithms are implemented for all the remaining sets. A cost function (CF) is evaluated in order to measure the convergence / proximity of the five simulated profiles for each parameter set. The following CF was found to be appropriate:

$$\begin{aligned}
 CF = \text{Mean}(&NSE(Z_{AZhb}(r), Z_{AZC}(r)), \\
 &NSE(Z_{AZC}(r), Z_{AZ\alpha}(r)), \\
 &NSE(Z_{AZC}(r), Z_{AZ0}(r)), \\
 &NSE(Z_{AZ\alpha}(r), Z_{AZ0}(r)), \\
 &NSE(PIA_{AZC}(r), PIA_{\Phi_{dp}}(r)), \\
 &NSE(PIA_{AZ0}(r), PIA_{\Phi_{dp}}(r)))
 \end{aligned}
 \tag{3.1}$$

where *Mean* stands for “the mean value of” and *NSE* is the Nash-Sutcliffe efficiency (Nash and Sutcliffe, 1970) between the two profiles indicated between brackets. The *NSE* criterion, or efficiency, is quite popular in hydrological sciences. It is employed in the context of parameter optimization since it has the definite advantage of being sensitive to both the average values and the correlation of the compared data series. Note that $NSE = 1$ denotes perfect agreement between the two series. The first four terms of the *CF* allow measuring the convergence of the four AZ reflectivity profiles that are different from each other (unlike the specific attenuation profiles of the *AZC* and *AZ α* algorithms, see section 2.2). Due to the inherent instability of the *AZhb* algorithm, we consider the first *NSE* term in the computation of the *CF* only if $PIA_m < 10$ dB. Indeed, this 10 dB value proved to be about the maximum value this algorithm is able to deal with, even with an almost perfect parameterization (Delrieu et al. 1999b). The last two terms of the *CF* are measuring the proximity of the polarimetric algorithm with the *AZC* and *AZ0* algorithms in terms



of the *PIA* profiles. Averaging *NSE* values computed for reflectivity and *PIA* profiles is acceptable since the ranges of variation of these two variables are of the same order of magnitude (note that this would not be the case for reflectivity and specific attenuation profiles). In the following, we have selected $CF_{th} = 0.8$ as the threshold to be exceeded to consider a given parameter set as “optimal”.

390

The acronyms *OPS* for “optimal parameter set” and *NOPS* for “number of optimal parameter sets” will be used hereinafter. The *NOPS* can be computed for a given target and time step and summed up for all the targets and time steps of an event and a series of events to yield a measure of the overall quality of a given simulation involving fixed parameters (b_{AZ} , b_{AK} , dC) and randomly drawn parameters (a_{AZ} , a_{AK} , $AF(r_0)$, dAF_m) for each single target / time step using the *LHS* technique. We recognise
395 that the choice of the cost function and the “satisfaction threshold” are essentially subjective. They rely on the experience gained during the implementing of the simulation framework. Two elements can be mentioned on this subject: (i) accounting for the *AZhb* algorithm for low to moderate *PIAs* less than 10 dB proved to be a good option owing to the strong sensitivity of this algorithm on the calibration error; (ii) adding the polarimetric algorithm and the subsequent last two *NSEs* in the *CF* allowed to dramatically reduce the mathematical ambiguity of the physical model at hand. This ambiguity is indeed quite large
400 for the *AZ* algorithms considered alone, in particular with regard to the dC , a_{AZ} and $AF(r_0)$ parameters.

3.2. Results

3.2.1 Illustration for a given target and time step

405

Figure 3 gives an example of result of the core procedure for target 13 (T13) on 21 July 2017 16:05 UTC. For this case with a MRT *PIA* of 25.9 dB at a range of about 20 km, we get $\Phi_{ap}(r_0, r_m) = 71.5^\circ$ and $Z_0 = 9.5$ dBZ. The optimal set of fixed parameters for the considered event is $dC^* = 0.4$ dB, $b_{AZ} = 0.78$ and $b_{AK}^* = 1.1$ (see next sub-sections). Since for the best *OPS*, all the reflectivity profiles overlap perfectly, the results presented in Fig.3 correspond actually to a less optimal set so
410 that one can see some differences between the solutions of the different algorithms. The set of optimal “*LHS*-sampled” parameters for this specific target / time step is $PIA_0^* = 0.46$ dB, $a_{AZ}^* = 1.01 \cdot 10^{-4}$, $a_{AK}^* = 0.34$ and $dAF_m^* = 0.99$. The *CF* value is 0.925, while the *CF* value obtained with the best *OPS* is 0.981. Note that 55 parameter sets overpassed the *CF* threshold value of 0.8 for this example, i.e. $NOPS = 55$. For this good (though not the best) *OPS*, the reflectivity profiles (Fig. 3a) call for the following comments. We have here a clear example of the inherent instability of the *AZhb* algorithm, which “blows up” at a range of about 7 km for this parameterization. One should remember that this algorithm is not accounted for in the *CF*
415 computation for such high *PIAs*, as explained in sub-section 3.1. The three other *AZ* algorithms give rather similar results. As a general behaviour (and in particular whatever the value of the on-site attenuation), we note that the optimal parameterizations lead to the convergence of the *AZC* and *AZO* algorithms near the radar and to the convergence of the *AZ α* and *AZO* algorithms



on the other end of the profile. Fig 3b gives the solutions obtained in terms of specific attenuation profiles. The $AZhb$ profile
420 is not drawn in this figure. As shown in sub-section 2.2, the $AZ\alpha$ and AZC solutions are identical (represented in red) and
slightly different at long range from the AZO solution. The comparison of the corrected and uncorrected profiles clearly shows
in this example the dramatic impact of attenuation as regard to both the underestimation of the first precipitation cell and the
non-detection of the second one. Fig. 3c displays the raw and processed Φ_{dp} profiles. For such a strong attenuation case, one
can see that the raw profile has little noise and no significant “bumps” that could sign a differential phase shift on backscattering
425 (δ_{hv}) contamination (Trömel et al., 2013). Finally, Fig. 3d allows comparison of the PIA profiles derived from the AZC - $AZ\alpha$
algorithms (identical solutions), the AZO algorithm and from the Φ_{dp} profile. Although there are some differences, the overall
consistency between the three profiles is good.

3.2.2 Time series of optimal parameter values

430

Figure 4 presents the time series of the input variables and optimal parameters obtained for the best simulation of the 21 July
2017 convective event. The second sampling strategy making use of Z_0 (see Table 1) is considered for PIA_0 in this example.
We will come back in sub-section 3.2.5 on the relationship between PIA_0 (Fig. 4c) and Z_0 (Fig. 4a). The time series of the
medians of PIA_m and $\Phi_{dp}(r_m)$ give an indication on the evolution of the storm intensity which was greater between 15:30
435 and 17:00 UTC with medians of about 20 dB and 60°, respectively. The interquartile ranges of these two variables are quite
large, as a result of both the variation of the radar-target distances (from 15 up to 40 km) and the precipitation variability as a
function of the azimuth, illustrated in Figs 1 and 2. The time evolution of the storm intensity is more marked on the $NOPS$
time series (Fig. 4f) with multiplicative factors in the range of 5 to 10 between the period 16:00-17:00 and the period 17:00-
18:00 UTC. Although for a given target, there is an increasing trend of $NOPS$ when PIA_m increases (not shown for the sake
440 of conciseness), this is also related to the higher number of targets “reached” (i.e. targets with PIA_m values greater than 1 dB)
between 16:00 and 17:00 UTC. We draw the attention of the reader to the low $NOPS$ values and to the singular values obtained
for the optimal parameters (Figs 4cde) at time step 17:00 UTC compared with the rest of the time series. This is related to the
strong on-site attenuation already evidenced on Fig. 2 (bottom graphs), which will be discussed in more detail in sub-section
3.2.5.

445

Some explanations are required at this stage regarding the choice made in the present simulation exercise for the values and
ranges of variation of the prefactors and exponents of the $A - Z$ and $A - K_{dp}$ relationships. Estimations were obtained from
the processing of the drop size distribution (DSD) data collected with a PARSIVEL 2 disdrometer located at the IGE site. The
dataset includes 337 rainy days during the period April 2017 – March 2020. The raw DSD measurements have a time resolution
450 of 1 min. They are binned into 32 diameter classes with increasing sizes from 0.125 mm up to 6 mm. Various filters (Hachani
et al. 2017) were applied to discard anomalous data and, in particular to detect non-liquid precipitation, thanks to the falling



speed spectra. The volumetric concentration spectra were then computed at a 5-min resolution. DSD spectra with 5-min rainrate less than 0.1 mm h^{-1} were discarded from the analysis. A dataset of about 14600 DSD spectra was thus obtained corresponding to all types of precipitation occurring in liquid phase in the Grenoble valley. As for the scattering model, we used the
455 CANTMAT version 1.2 software programme that was developed at Colorado State University by C. Tang and V.N. Bringi. The CANTMAT software uses the T-Matrix formulation to compute radar observables such as horizontal reflectivity, vertical reflectivity, differential reflectivity, co-polar cross-correlation, specific attenuation, specific phase shift, etc, as a function of the DSD, the radar frequency, air temperature, oblateness models and canting models for the raindrops as well as the incidence angle of the electromagnetic waves. The results presented herein were computed for the X-band frequency, a temperature of
460 10°C , the Beard and Chung (1986) oblateness model, a standard deviation of the canting angle of 10° and an incidence angle of 0° (horizontal scanning, like for the MOUC radar data).

Figure 5 illustrates the fittings of the $A - Z$ relationship obtained from a classical logarithm of base 10 transformation of the two variables. One can note that the scatterplot is well conditioned for deriving a power-law model in the sense that it does not
465 present any particular curvature. The models provide good fits for the highest values, which correspond to convective rainfall. The determination coefficient is high and the three regressions performed give subsequently parameter sets close to each other. Our choice is to select the least-rectangle fit since for these calculations based on DSD data, the two variables can be considered in an equal footing. From this analysis, we have chosen (Table 1) $b_{AZ} = 0.78$ as a fixed value for this exponent and $a_{AZ} = 1.0 \cdot 10^{-4}$ as the central value for the *LHS* sampling of the prefactor. Although the scatter of the points around the power-law
470 model suggests a possible range of variation of $[-5, 5 \text{ dB}]$ for the DSD-derived values, we have limited this range to $[-3, 3 \text{ dB}]$ in our simulations on the basis of the much bigger resolution volume of the radar and the assumption that the prefactor is constant throughout the reflectivity profile.

Figure 6 gives the results obtained for the $A - K_{dp}$ relationship. It can be seen that the scatterplot of the logarithmic of base
475 10 transformed variables (Fig. 6a) presents a significant curvature. Due to the important weight given to low and medium values, the fitted power-law models are clearly unsatisfactory for the highest values, which are of interest in the present study. We have therefore tested two other fitting techniques based on the natural values of the two variables (Fig. 6b). A linear fit with a 0-forced intercept yields $A_h = 0.32 K_{dp}$ which is consistent with linear relationships proposed in the literature (Schneebeli et al. 2013). However, once again, we note that this linear fit is not good for the highest values. The fitting of a
480 non-linear power-law model (*NLPL*) proves to be more satisfactory with $A_h = 0.30 K_{dp}^{1.1}$. Since the exponents estimated with the log-transformed data are close to 0.9, we have decided to perform several simulations with fixed values of b_{AK} in the range $[0.9 - 1.2]$ (see Table 1). Regarding the prefactor a_{AK} , we have considered a central value of 0.3 and a range of variation of $[-3, 3\text{dB}]$, that is minimum and maximum values of 0.15 and 0.6, respectively.



485 Additional sensitivity tests can be performed on such DSD-derived relationships, including for instance the influence of the
air / hydrometeor temperature, the precipitation type (e.g. stratiform versus convective rainfall), the DSD integration time step,
etc. Concerning the last factor, we compared the results obtained for the 2-min and 5-min time steps and we found no significant
influence on the coefficients of the power-law models, while the R^2 values were significantly downgraded for the 2-min time
step (not shown here for the sake of conciseness). As for the precipitation type, we carried out a rough classification of the 337
490 events into stratiform and convective types, by considering an event as convective if a rainrate threshold of 10 mm h^{-1} was
exceeded for at least one 5-min time step during the event. As one would expect from the scatterplots in Figs 5 and 6, significant
differences appeared between the stratiform and convective $A - K_{dp}$ relationships whereas the $A-Z$ relationships were almost
identical. This is an argument for keeping the exponent b_{AZ} constant in the simulation procedure. Regarding the sensitivity on
temperature, one possible extension of the present work could be to consider the temperature time series available for each
495 event at the IGE site in the scattering calculations. This would most likely result in an increase of the variability of the $A-Z$ and
 $A - K_{dp}$ relationships. As a classical concern, one may however wonder how the average temperature in the radar resolution
volume could be estimated (Ryzhkov et al. 2014). We chose herein to rely on the ability of the simulation procedure to deviate
from the central values of the parameters and their ranges of variation to be large enough.

500 The time series of the prefactors a_{AK} (Fig. 4d) and a_{AZ} (Fig. 4e) exhibit similar behaviour with (i) median values close to the
central values for the most intense part of the event between 16:00 and 16:50 UTC as well as between 17:15 and 17:45, (ii)
significant deviations for the most on-site attenuation prone time steps (lower medians between 15:30 and 16:00 UTC and
higher median at 17:00 UTC) and (iii) more erratic behaviour from one step to the next after 17:45 UTC at the end of the
storm. The first point in the previous list is reassuring in terms of the possibility of using DSD-derived power-law models, and
505 particularly the DSD-derived $A-R$ relationship, for radar QPE. The second point is difficult to explain from a physical point of
view. Coupled with the observation that the interquartile ranges are quite large, especially those of the a_{AZ} parameter, we
believe that the mathematical ambiguity (Haddad et al., 1995) of the system of equations at hand remains important. It is
noteworthy to mention that the mathematical ambiguity of the AZ algorithms alone is much larger (e.g. with larger interquartile
ranges for the a_{AZ} parameter). Introducing the constraints related to the polarimetric algorithm allowed to reduce it
510 dramatically.

3.2.3 Estimating the radar calibration error

In order to increase the robustness of the results, the simulation procedure was performed for three convective events that
515 occurred successively during summer 2017. Table 2 presents some characteristic features of these events. For all of them the
melting layer (ML) altitude, determined with the 25° -elevation XPORT radar data by using the procedure developed in Khanal
et al. 2019, was situated well above the altitude of the Moucherotte Mount radar, hence, there is no ML contamination of the
considered radar data. The first two events were rather intense and similar in terms of total rain amount and maximum rainrate



at the IGE site, as well as in terms of the PIA_m statistics based on the 22 mountain targets. The third one was a bit less intense.
520 To our knowledge, there was no occurrence of hail reported in the area of interest for these three events.

Figure 7 shows the evolution of $NOPS$ for the three events separately and all together as a function of the fixed values of dC listed in Table 1. The optimal values of the other fixed parameters are considered in these results with $b_{AZ} = 0.78$ and $b_{AK}^* = 1.1$. We note that the various curves are rather flat near their optimum values, e.g. with a ratio between the maximum $NOPS$ value and the nearest value, 0.4 dB apart, of 1.02 when the data of the three events are grouped. The overall sensitivity of the
525 dC parameter is clear however in the considered $[-2, 2$ dB] range, e.g. with a ratio of the maximum to the minimum $NOPS$ values of 2.04 for the all-events curve. Although the global results tend to indicate a very slight underestimation of the measured reflectivities, one can note that the optimal dC values vary from one event to the next. The 21 July 2017 event is different from the other two and the results suggest on the contrary a slight overestimation of the reflectivities in that case. We
530 find it difficult to know whether such variations in the electronic calibration of the radar from one event to the next could be physically realistic. In any case, an in-depth analysis of the time series showed that on-site attenuation could not be held responsible for this result.

3.2.4 Linearity of the $A - K_{dp}$ relationship

535 Figure 8 shows the simulation results for the series of b_{AK} values listed in Table 1. We note a slight superiority of the simulation with $b_{AK} = 1.1$ compared to the one with $b_{AK} = 1.0$ in terms of the maximum value of the $NOPS$ computed over the three events all together. This observation is also valid for each of the 3 events separately (not shown). The simulation with $b_{AK} = 0.9$ is clearly below the other two. For $b_{AK} = 1.1$, the log-transformed distribution of a_{AK} computed over the three events is
540 nearly symmetrical with an average value of 0.275 and an interquartile range of nearly $[-1, 1$ dB]. Hence, we obtain in this study quite a remarkable agreement between the radar and DSD-derived $A - K_{dp}$ relationships for convective precipitation, with $A = 0.275 K_{dp}^{1.1}$ and $A = 0.30 K_{dp}^{1.1}$, respectively.

3.2.5 Radome attenuation

545 Coming back to Figure 4, we remind that the second sampling strategy making use of Z_0 was considered for the random drawing of PIA_0 values in this simulation. With $n = 3.0$, the crude model proposed in Table 1 yields upper limits of the PIA_0 sampling range of 3.0, 5.8, 9.2 and 13.1 dB for Z_0 values of 20, 30, 40 and 50 dBZ, respectively. One has to remark that such close-range reflectivity measurements are actually affected by radome attenuation. This may explain why estimated PIA_0
550 values are of the same order of magnitude for time step 17:00 UTC than for time steps between 15:30 and 15:55 while Z_0 values are about 10 dBZ higher in this second period. Thus the relevance of the Z_0 variable for detection and quantification of



on-site attenuation may remain limited for a radar equipped with a radome. Nevertheless, Figure 7 shows the comparison of the two PIA_0 sampling strategies making use or not of Z_0 (blue and red continuous curves), by reference to the $NOPS$ variable computed for the three convective events. This figure clearly evidences a superiority of the strategy taking into account, even
555 in a crude manner, the precipitation conditions at the radar site.

Figure 9 gives two examples of the core procedure implementation in the case of severe on-site attenuation that occurred on 21 July 2017 at 17:00 UTC (Fig. 2 bottom graphs). The constraint on the PIA_0 sampling model was relaxed by considering $n = 10$ in the model of Table 1, that is upper limits of PIA_0 sampling range of 15.2 and 29.1 dB for Z_0 values of 30 and 40
560 dBZ, respectively. The returns from Target 04 (T04) allow to quantify both on-site attenuation and along-path attenuation due to precipitation falling over the city of Grenoble (NE sector) at that time (left-hand side example). At this range of about 40 km, we get $PIA_m = 47.9$ dB and $\Phi_{dp}(r_0, r_m) = 129.9^\circ$. The returns from Target 19 (T19) located in the South-East sector (right-hand side) seem to be essentially affected by the precipitation conditions at the radar site. At this range of about 27 km, we get $PIA_m = 11.9$ dB and $\Phi_{dp}(r_m) = 12.2^\circ$. This yields $PIA_m/\Phi_{dp}(r_0, r_m)$ ratios of 0.37 and 0.97 dB degree⁻¹ for the
565 two targets, respectively. These values are clearly (especially the second one) well above the range of expected values for the slope of a supposedly linear $A - K_{dp}$ relationship (Schneebeli et al. 2013), which in addition to the generalized decrease of the mountain returns, is an indication of a significant on-site attenuation effect. The dC -corrected Z_0 values computed in the directions of the two targets are significantly different with 38.9 and 28.6 dBZ, respectively. One can observe the very good convergence of all the AZ algorithms in both cases. In particular for T19, all the AZ reflectivity profiles, including the AZ_{hb}
570 one, are perfectly matched. The agreement is also very good between the PIA profiles of the AZ algorithms and the one of the polarimetric algorithm, except for a very slight stall of $PIA_{\Phi_{dp}}(r)$ at a range of about 30 km for T04, likely due to disturbances associated with side-lobe effects (visible on the ρ_{nv} PPI on top of Fig. 9).

For the two OPS considered in Fig. 9, one gets PIA_0 values 10.1 and 10.8 dB. By considering the PIA_0 statistical distribution calculated over the optimal parameter sets of all the targets for the considered time step, one obtains a symmetrical distribution
575 with a slightly higher mean value of 12.6 dB and a rather large interquartile range of 4.5 dB. The mean value increases somehow (13.5 dB) and the interquartile range decreases to 3.2 dB if the PIA_0 distribution is computed for targets 9-22 only, i.e. for targets with reduced along-path attenuation. It is worth noting that such statistics are not improved (e.g., interquartile range reduced) if one considers a more stringent satisfaction criterion (e.g. $CF_{th} = 0.9$ instead of $CF_{th} = 0.8$).

580

4. Discussion and future work

In this paper, we have started to implement a global approach to study the interactions between X-band microwaves and hydrometeors in a mountainous context. Emphasis was placed on the attenuation problem, which is known to be severe for the



585 frequency under consideration and essentially uncorrectable unless estimates of total attenuation are available at a distance
from the radar. The RadAlp experiment allows us to obtain direct PIA estimates from the Mountain Reference Technique in
some specific directions and indirect estimates from the processing of the profiles of total differential phase shift available for
each radial. Although the polarimetric technique is *a priori* much more convenient to apply and has interesting characteristics
(independence on radar calibration, on-site attenuation and partial beam blockages), it suffers from several limitations,
590 including (i) the fact that the Ψ_{dp} profile is noisy for light precipitation, (ii) possible contaminations by the differential phase
shift on propagation δ_{hv} (ii) possible impact of non-uniform beam filling and (iii) the need to specify the relationship between
the specific attenuation and the specific differential phase shift which depends on hydrometeor types, temperature, and so on.
In a similar way to the satellite configuration (e.g. the possibility to use the Surface Reference Technique in addition to the
dual-frequency measurements at Ka and Ku Bands for processing the radar data of the GPM core platform ; Meneghini et al.
595 2020), we have proposed to take advantage of all the MRT and polarimetric measurements available to perform a generalized
sensitivity analysis of the physical model of interest. In the simple case of convective precipitation, we obtained interesting
results regarding the radar calibration, the radome attenuation and the coefficients of the $A - Z$ and $A - K_{dp}$ relationships. We
note that for the estimated optimal radar calibration error, the $A - Z$ and $A - K_{dp}$ relationships derived from radar data are consistent
with those derived from concomitant drop size distribution measurements at ground level, in particular with a slightly non-
600 linear $A - K_{dp}$ relationship ($A = 0.275 K_{dp}^{1.1}$). This is reassuring regarding the relevance of microphysical data and scattering
models for the radar QPE parameterization. We have deliberately left aside the question of the specific attenuation - rainrate
conversion in this article. An interesting validation exercise to be performed consists in using the DSD-derived $A - R$
relationship for the conversion of the estimated specific attenuation profiles; then these radar rainrate estimates will be
compared with the raingauge measurements available. Another outcome of the study is the quantification of X-Band radome
605 attenuation. Values as high as 15 dB were estimated, leading to the recommendation of avoiding the use of radomes for remote
sensing of precipitation at such frequency. As an alternative, it would be desirable to develop specific sensors to detect /
quantify the presence of water on the radome wall. The study showed that the measured reflectivity at the radar site is not a
good predictor for radome attenuation. As a next step, we plan to extend the procedure to stratiform events with MOUC radar
measurements made at times within or above the melting layer. The multi-angle, multi-frequency, polarimetric measurements
610 of the valley-based radars will be critical in this respect for the characterization of the ML from below (Khanal et al. 2019,
2022) and the mitigation of the mathematical ambiguity of the physical model of interest.

615



Code and data availability

620 There will be no problem to make available at a later stage the codes / data developed / used in this study, preferably through
demands of collaboration to the authors.

Conflict of interest

The authors declare that they have no conflict of interest.

625

Author contribution

GD is the main contributor for this article (concept, theoretical developments, calculations, article writing, corresponding
author). AKK (PhD student) and BB (assistant professor) are scientists contributing actively to the RadAlp experiment. They
performed the internal review of the article. FC is a research engineer who built and keeps improving the XPORT radar, a key
630 instrument deployed in the RadAlp experiment. BB is also the HMCIS team leader and as such does a lot of work for the team
members.

Acknowledgements

We are grateful to P.N. Gatlin (NASA Marshall Space Flight Center, Huntsville, AL) for providing the CANTMAT version
635 1.2 software developed at Colorado State University by C. Tang and V.N. Bringi, who we also thank. The RadAlp experiment
is co-funded by the Labex osug@2020 of the Observatoire des Sciences de l'Univers de Grenoble, the Service Central
Hydrométéorologique et d'Appui à la Prévision des Inondations (SCHAPI) and Electricité de France / Division Technique
Générale (EDF/DTG).

References

- 640 Beard, K.V., and Chuang, C.: A new model for the equilibrium shape of raindrops, *J. Atmos. Sci.*, 44, 1509-1524.
[https://doi.org/10.1175/1520-0469\(1987\)044<1509:ANMFTE>2.0.CO;2](https://doi.org/10.1175/1520-0469(1987)044<1509:ANMFTE>2.0.CO;2), 1987.
- Bringi, V.N., and Chandrasekar, V.: *Polarimetric Doppler weather radar, principles and applications*. Cambridge University
Press, 636 pp, 2001.
- 645 Delrieu, G., Caoual, S., Creutin, J.D.: Feasibility of using mountain return for the correction of ground-based X-band
weather radar data. *J. Atmos. Oceanic Technol.*, 14(3), 368-385 DOI: 10.1175/1520-
0426(1997)014<0368:FOUMRF>2.0.CO;2, 1997.
- 650 Delrieu, G., Serrar, S., Guardo, E., and Creutin, J.D.: Rain Measurement in Hilly Terrain with X-Band Weather Radar
Systems: Accuracy of Path-Integrated Attenuation Estimates Derived from Mountain Returns. *J. Atmos. Oceanic Technol.*,
16, 405–416, [https://doi.org/10.1175/1520-0426\(1999\)016<0405:RMIHTW>2.0.CO;2](https://doi.org/10.1175/1520-0426(1999)016<0405:RMIHTW>2.0.CO;2), 1999.



- 655 Delrieu, G., Hucke, L., and Creutin, J.D.: Attenuation in rain for X- and C-band weather radar systems: Sensitivity with respect to the drop size distribution. *Journal of Applied Meteorology* 38(1): 57-68. [https://doi.org/10.1175/1520-0450\(1999\)038<0057:AIRFXA>2.0.CO;2](https://doi.org/10.1175/1520-0450(1999)038<0057:AIRFXA>2.0.CO;2), 1999b.
- 660 Delrieu, G., Khanal, A.K., Yu, N., Cazenave, F., Boudevillain, B., and Gaussiat, N.: Preliminary investigation of the relationship between differential phase shift and path-integrated attenuation at the X band frequency in an Alpine environment. *Atmos. Meas. Tech.*, 13, 3731–3749, <https://doi.org/10.5194/amt-13-3731-2020>, 2020
- 665 Foresti, L., Sideris, I.V., Panziera, L., Nerini, D., and Germann, U.: A 10-year radar-based analysis of orographic precipitation growth and decay patterns over the Swiss Alpine region. *Q. J. R. Meteorol. Soc.*, 144(176), 2277-2301, DOI: 10.1002/qj.3364, 2018.
- 670 Frasier, S.J., Kabeche, F., Figueras i Ventura, J., Al-Sakka, H., Tabary, P., Beck, J. and Bousquet, O.: In-place estimation of wet radome attenuation at X band. *J. Atmos. Oceanic Technol.*, 30, 917–928, <https://doi.org/10.1002/qj.3366>, 2013.
- Germann, U., Galli, G., Boscacci, M., and Bolliger, M.: Radar precipitation measurement in a mountainous region. *Q. J. Royal Meteorol. Soc.*, 132(618), 1669-1692; DOI: 10.1256/qj.05.190, 2006.
- Haddad, Z.S., Im, E., and Durden, S.L.: Intrinsic ambiguities in the retrieval of rain rates from radar returns at attenuating wavelengths. *Journal of Applied Meteorology and Climatology*, 1995, vol. 34, no 12, p. 2667-2679.
- 675 Joss, J. and Lee, R.: The Application of Radar-Gauge Comparisons to Operational Precipitation Profile Corrections. *J. Appl. Meteor.*, 34, 2612–2630, [http://dx.doi.org/10.1175/1520-0450\(1995\)034<2612:TAORCT>2.0.CO;2](http://dx.doi.org/10.1175/1520-0450(1995)034<2612:TAORCT>2.0.CO;2), 1995.
- 680 Khanal, A. K., Delrieu, G., Cazenave, F., and Boudevillain, B.: Radar remote sensing of precipitation in high mountains: detection and characterization of Melting Layer in French Alps, *Atmosphere*, 10, 784; doi:10.3390/atmos10120784, 2019.
- Khanal, A. K., Delrieu, G., Cazenave, F., and Boudevillain, B.: Investigation of the relationship between path-integrated attenuation (PIA) and differential phase shift (Φ_{dp}) in the melting layer of precipitation at X-band frequency. Submitted to *Atmospheric Measurement Techniques*, January 2022.
- 685 Koffi, A.K, Gosset, M., Zahiri, E.-P., Ochou, A.D., Kacou, M., Cazenave, F., and Assamoi, P.: Evaluation of X-band polarimetric radar estimation of rainfall and rain drop size distribution parameters in West Africa. *Atmospheric Research*, 143, 438–461. DOI:10.1016/j.atmosres.2014.03.009, 2014.
- 690 Lengfeld, K., Clemens, M., Münster, H., and Ament, F., 2014: Performance of high-resolution X-band weather radar networks – the PATTERN example, *Atmospheric Measurement Techniques*, 7, 4151–4166, <https://doi.org/10.5194/amt-7-4151-2014>.
- 695 Marzoug, M., and Amayenc, P.: A class of single and dual-frequency algorithms for rain-rate profiling from a spaceborne radar: Part 1- Principle and tests from numerical simulations. *J. Atmos. Oceanic Technol.*, 11, 1480-1506. [http://dx.doi.org/10.1175/1520-0426\(1994\)011%3C1480:ACOSAD%3E2.0.CO;2](http://dx.doi.org/10.1175/1520-0426(1994)011%3C1480:ACOSAD%3E2.0.CO;2), 1994.
- Matrosov, S. Y., and Clark, K.A.: X-Band Polarimetric Radar Measurements of Rainfall. *J. Appl. Meteor.* 41(9): 941-952. [http://dx.doi.org/10.1175/1520-0450\(2002\)041%3C0941:XBPRMO%3E2.0.CO;2](http://dx.doi.org/10.1175/1520-0450(2002)041%3C0941:XBPRMO%3E2.0.CO;2), 2002.
- 700 Matrosov, S.Y., Kingsmill, D.E., Martner, B.E., and Ralph, F.M.: The Utility of X-Band Polarimetric Radar for Quantitative Estimates of Rainfall Parameters. *J. Hydrometeor.*, 6, 248–262, <https://doi.org/10.1175/JHM424.1>, 2005.



- 705 Matrosov, S.Y., Campbell, C., Kingsmill, D.E., and Sukovich, E.: Assessing Snowfall Rates from X-Band Radar Reflectivity Measurements. *J. Atmos. Oceanic Technol.*, 26, 2324–2339, DOI: 10.1175/2009JTECHA1238.1, 2009.
- Meneghini, R., J. Eckermann, and Atlas, D.: Determination of rain rate from a space borne radar using measurements of total attenuation. *IEEE Transactions in Geosciences and Remote Sensing*, GE-21, 34-43, 1983.
- 710 Meneghini, R., H. Kim, L. Liao, J. Kwiatkowski, and T. Iguchi, 2020: Path attenuation estimates for the GPM Dual-frequency Precipitation Radar (DPR). *J. Meteor. Soc. Japan*, 99, 181–200, doi:10.2151/jmsj.2021-010
- McLaughlin, D., Pepyne, D., Chandrasekar, V., Philips, B., Kurose, J., Zink, M., Droegemeier, K., Cruz-Pol, S., Junyent, F., Brotzge, J., Westbrook, D., Bharadwaj, N., Wang, Y., Lyons, E., Hondl, K., Liu, Y., Knapp, E., Xue, M., Hopf, A., Kloesel, K., DeFonzo, A., Kollias, P., Brewster, K., Contreras, R., Dolan, B., Djaferis, T., Insanic, E., Frasier, S., and Carr, F.: Short-Wavelength Technology and the Potential For Distributed Networks of Small Radar Systems, *Bulletin of the American Meteorological Society*, 90, 1797–1818, <https://doi.org/10.1175/2009BAMS2507.1>, 2009.
- 715 Park, S.-G., Bringi, V. N., Chandrasekar, V., Maki, M., and Iwanami, K., 2005. Correction of Radar Reflectivity and Differential Reflectivity for Rain Attenuation at X Band. Part I: Theoretical and Empirical Basis, *Journal of Atmospheric and Oceanic Technology*, 22, 1621–1632, <https://doi.org/10.1175/JTECH1803.1>, 2005.
- 720 Ryzhkov, A.V., Giangrande, S.E., and Schuur, T.J.: Rainfall estimation with a polarimetric prototype of WSR-88D. *J. Appl. Meteor.*, Vol. 44, Issue 4, p502-515. DOI: 10.1175/JAM2213.1, 2005.
- 725 Ryzhkov, A. V., Diederich, M., Zhang Pengfei, and Simmer, C.: Potential utilization of specific attenuation for rainfall estimation, mitigation of partial beam blockage and radar networking. *J. Atmos. Oceanic Technol.*, Vol. 31, p599-619. DOI: 10.1175/JTECH-D-15-00038.1, 2014.
- 730 Saltikoff, E., G. Haase, L. Delobbe, N. Gaussiat, M. Martet, D. Idziorek, H. Leijnse, P. Novák, M. Lukach, and K. Stephan, 2019. OPERA the Radar Project. *Atmosphere*, 10, 320; doi:10.3390/atmos10060320.
- Saxion, D. S., and Coauthors, 2011: New science for the WSR-88D: Validating the dual polarization upgrade. 27th International Conference on Interactive Information Systems Processing for Meteorology, Oceanography, and Hydrology, Jan 22-27, 2011, Seattle, WA, USA.
- 735 Schneebeli, M., and Berne, A.: An Extended Kalman Filter Framework for Polarimetric X-Band Weather Radar Data Processing. *J. Atmos. Oceanic Technol.*, 29, 711–730, <https://doi.org/10.1175/JTECH-D-10-05053.1>, 2012.
- 740 Scipion, D. E., R. Mott, M. Lehning, M. Schneebeli, and A. Berne (2013), Seasonal small-scale spatial variability in alpine snowfall and snow accumulation, *Water Resour. Res.*, 49, 1446–1457, doi:10.1002/wrcr.20135.
- Serafin, R. J., and J. W. Wilson, 2000: Operational weather radar in the United States: Progress and opportunity. *Bull. Amer. Meteor. Soc.*, 81, 501–518.
- 745 Serrar, S., Delrieu, G., Creutin, J.D., Uijlenhoet, and R.: Mountain Reference Technique: Use of mountain returns to calibrate weather radars operating at attenuating wavelengths. *J. Geophys. Res. – Atmospheres*, 105(D2): 2281-2290. DOI :10.1029/1999JD901025, 2000.
- 750 Sideris, I. V., Gabella, M., Erdin, R., and Germann, U.: Real-time radar–raingauge merging using spatio-temporal co-kriging with external drift in the alpine terrain of Switzerland. *Q. J. R. Meteorol. Soc.*, 140, 1097 – 1111, DOI:10.1002/qj.2188S, 2014.



- 755 Testud, J, Le Bouar, E., Obligis, E. and Ali-Mehenni, M.: The Rain Profiling Algorithm Applied to Polarimetric Weather Radar. *J. Atmos. Oceanic Technol.*, 17: 332-356. [http://dx.doi.org/10.1175/1520-0426\(2000\)017%3C0332:TRPAAT%3E2.0.CO;2](http://dx.doi.org/10.1175/1520-0426(2000)017%3C0332:TRPAAT%3E2.0.CO;2), 2000.
- Trömel, S., Kumjian, M.R., Ryzhkov, A.V., Simmer, C., and Diederich, M.: Backscatter differential phase – estimation and variability. *J. Appl. Meteor. Climatol.*, 52, 2529-2548, doi: 10.1175/JAMC-D-13-0124.1, 2013.
- 760 Westrelin, S., Meriaux, P., Tabary, P., and Aubert Y.: Hydrometeorological risks in Mediterranean mountainous areas - RHYTMME Project: Risk Management based on a Radar Network. ERAD 2012 7th European Conference on Radar in Meteorology and Hydrology, June 2012, Toulouse, France. 6 p., hal-01511157, 2012.
- 765 Yu, N., Gaussiat, N., and Tabary, P.: Polarimetric X-band weather radars for quantitative precipitation estimation in mountainous regions. *Q. J. Royal Meteorol. Soc.*, 144(717), DOI:10.1002/qj.3366, 2018.

770



Table 1: Values and ranges of variation of the attenuation model parameters in the sensitivity analysis

Parameters fixed for a given simulation			
Parameter	Value(s)		
b_{AZ}	0.78		
b_{AK}	0.9, 1.0, 1.05, 1.10, 1.15, 1.20		
dC	[-2, 2 dB] with a step of 0.4 dB		
Parameters taken into account in the Latin Hypercubes Sampling for a given simulation			
Parameter	Central value	Range of multiplicative coefficient of the central value (in dB)	Lower and upper limit
a_{AZ}	$1.0 \cdot 10^{-4}$	[-3, 3 dB]	$[0.5 \cdot 10^{-4}, 2.0 \cdot 10^{-4}]$
a_{AK}	0.3	[-3, 3 dB]	[0.15, 0.6]
dAF_m	1.0	[-1, 1 dB]	[0.79, 1.26]
$AF(r_0)$: sampling #1	0.316	[-5, 5 dB]	$AF(r_0)$: [1.0, 0.1] corresponding to PIA_0 : [0, 10 dB]
$AF(r_0)$: sampling #2	$PIA_0^* = 0.0126 Z_0^{1.6}$ PIA_0^* [dB]; Z_0 [dBZ] $AF^*(r_0) = 10^{-PIA_0^*/10}$		Lower limits: $PIA_0^L = 0$; $A(r_0)^L = 1$ Upper limits: $PIA_0^U = n PIA_0^*$ $A(r_0)^U = 10^{-PIA_0^U/10}$ with $n = 3$ in results of Figs 3-4; 7-8 and $n = 10$ in results of Figs. 9-10

775



Table 2. Some characteristics of the three convective events considered in this study. The melting layer (ML) detection was performed with the 25°-elevation angle measurements of the XPORT radar using the algorithm described in Khanal et al. (2019). The total rain amount and the maximum rainrate are recorded at the raingauge available at the IGE site at the bottom of the Grenoble valley. The PIA_m statistics are derived from the MRT by considering all the 22 mountain targets and the 0° elevation data of the Moucherotte Mount radar.

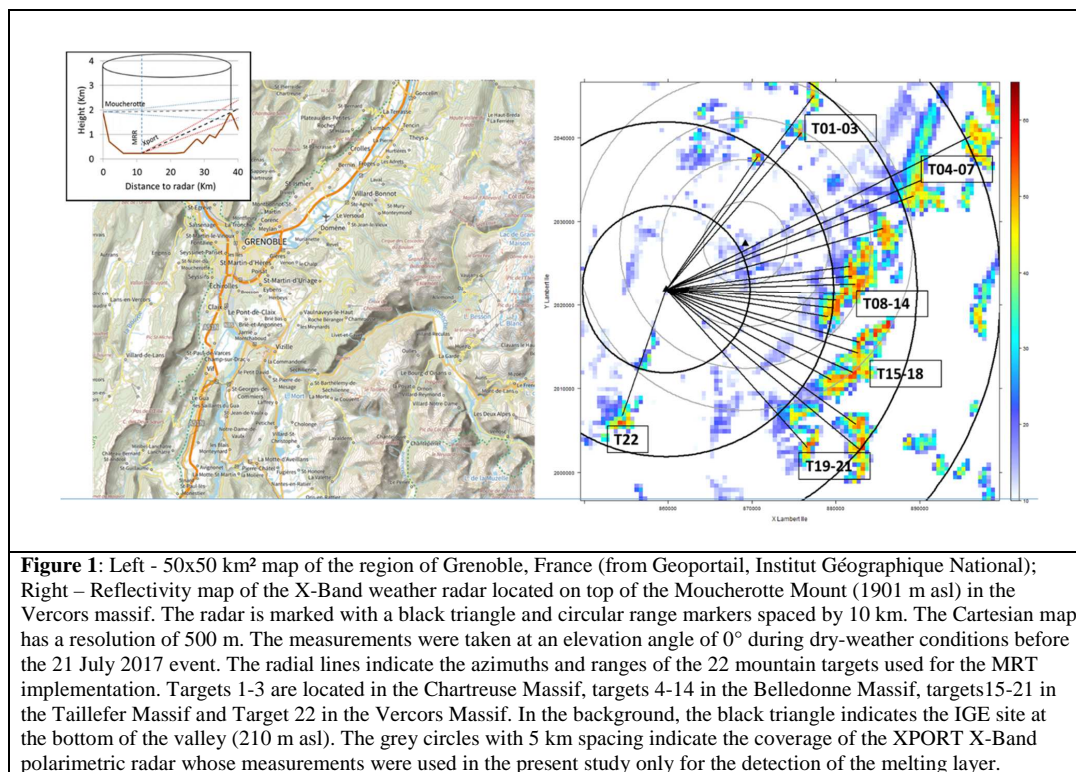
Date	Beginning (UTC)	End (UTC)	Minimum altitude of the ML bottom (m asl)	Total rain amount (mm)	Maximum rainrate in 10 min (mm h^{-1})	Maximum PIA_m value (dB)	Number of profiles with PIA_m greater than a given value
21 July 2017	15:30	19:00	3000	35.2	42.0	59.8	11 (> 40 dB)
8 August 2017	8:30	14:00	3700	27.9	48.0	63.4	20 (> 40 dB)
31 August 2017	7:00	11:30	3200	19.9	15.5	17.5	8 (> 15 dB)

785

790

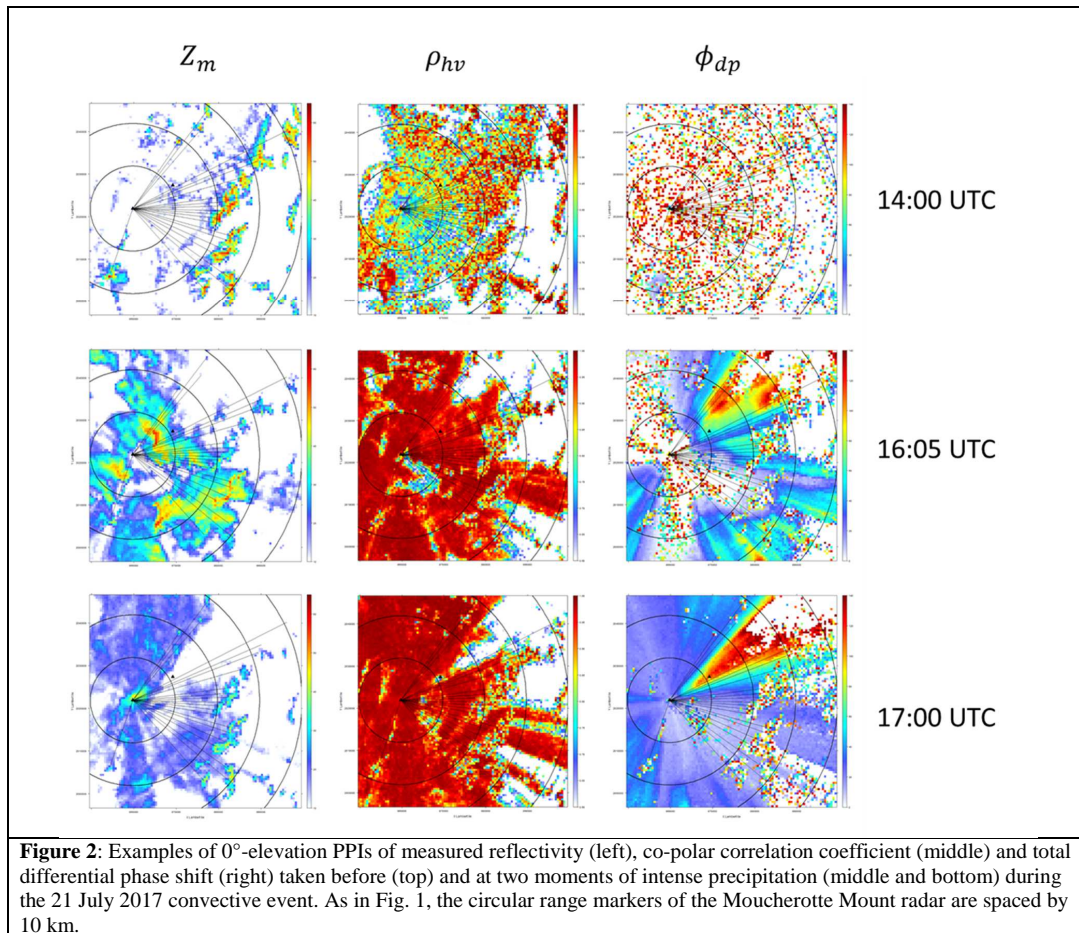


795





800





805

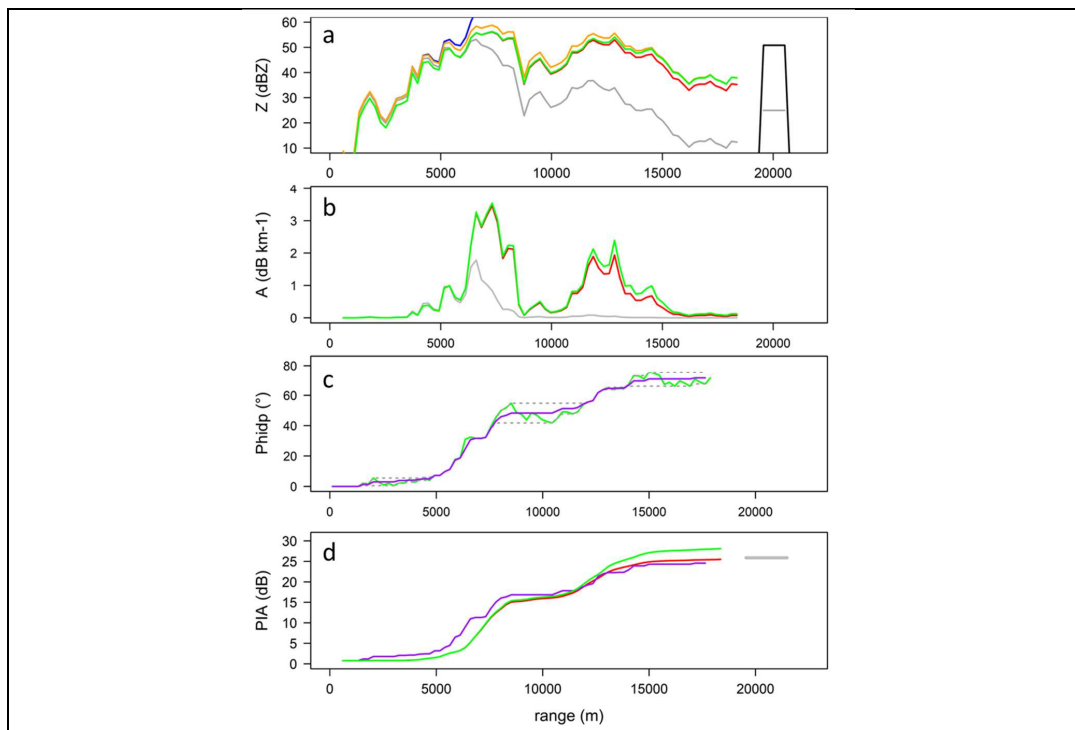
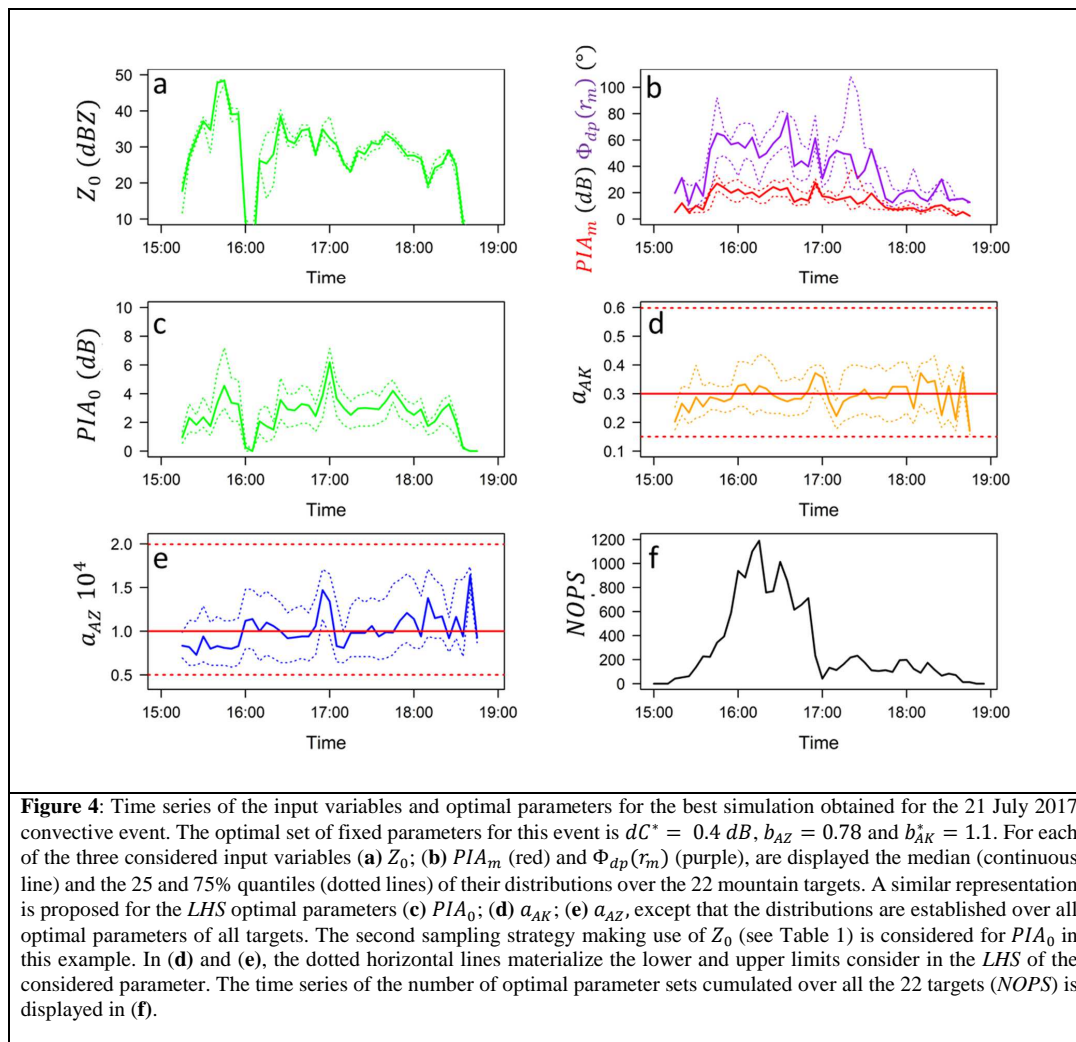
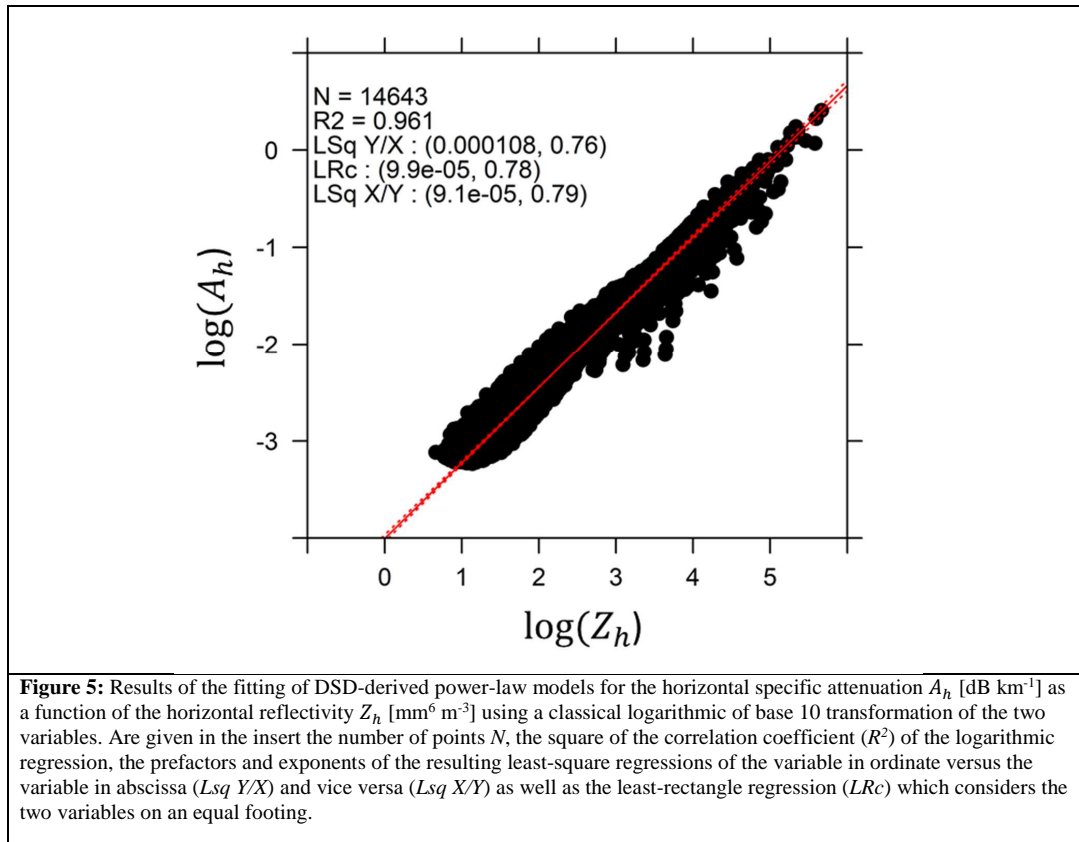
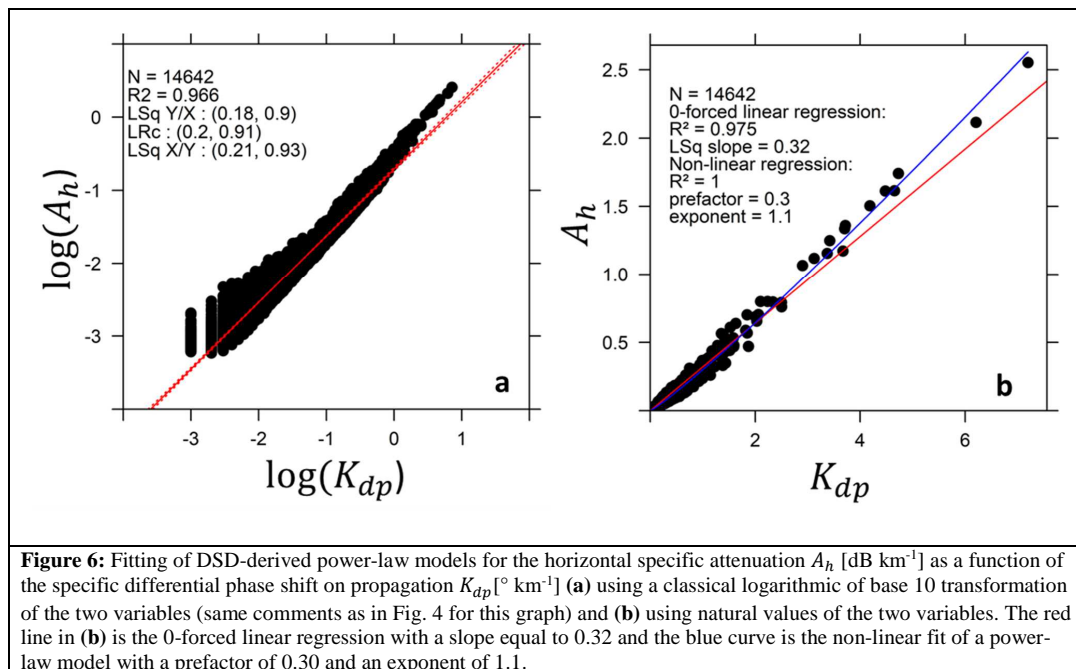


Figure 3: Implementation of the five algorithms (blue: $AZhb$; red: AZC ; orange: $AZ\alpha$; green: AZO ; purple: $PIA_{\phi dp}$) for mountain target T13 during the 21 July 2017 convective event at 16:00 UTC using a near-optimal parameter set (see text for details). The results are displayed in terms of profiles of (a) reflectivity, (b) specific attenuation, (c) differential phase shift on propagation and (d) path-integrated attenuation. The grey profile in (a) is the measured reflectivity profile; the black and grey horizontal lines at range 20 km represent the mean dry-weather baseline and current reflectivities, respectively, of the mountain target. The resulting measured PIA value of 25.2 dB is reported in grey in (d). The grey profile in (b) is derived from the measured reflectivity profile by using eq. 2.5. The black line in (c) is the raw total differential phase shift profile and the grey dotted lines are the envelope curves used in the regularization procedure (Delrieu et al. 2020, Khanal et al. 2022).

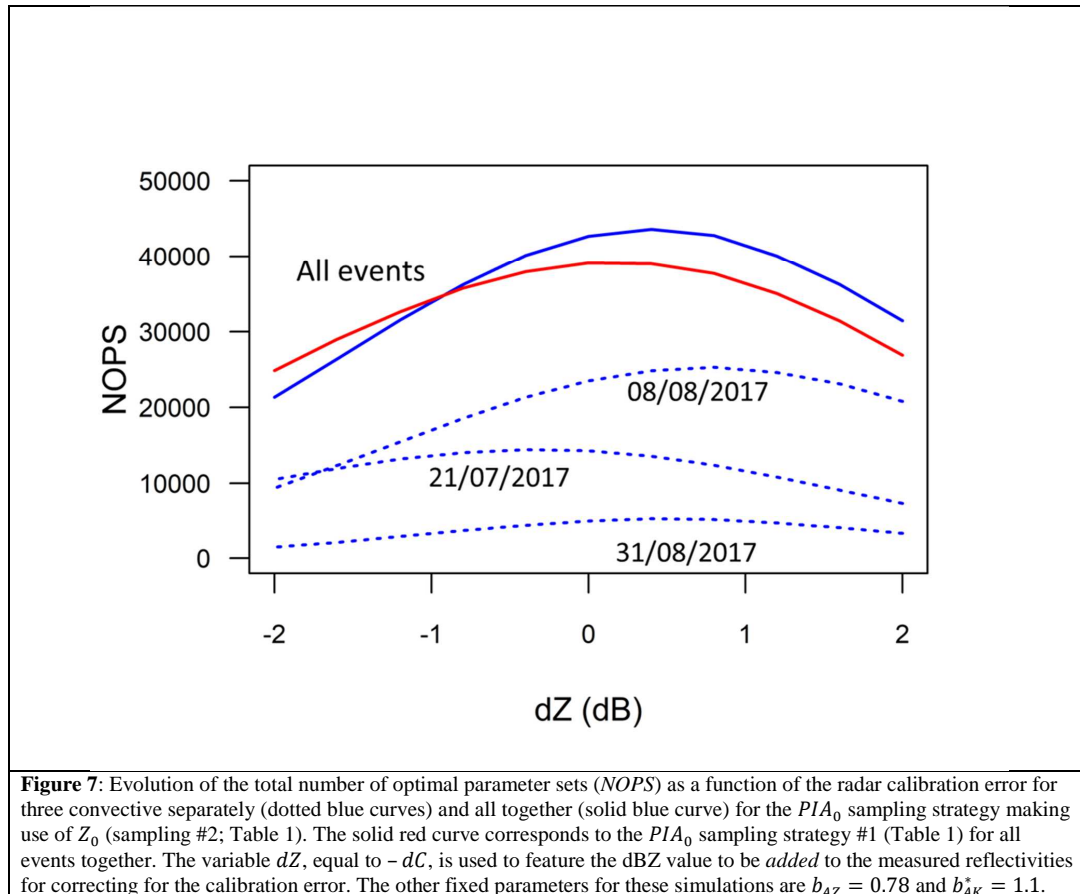


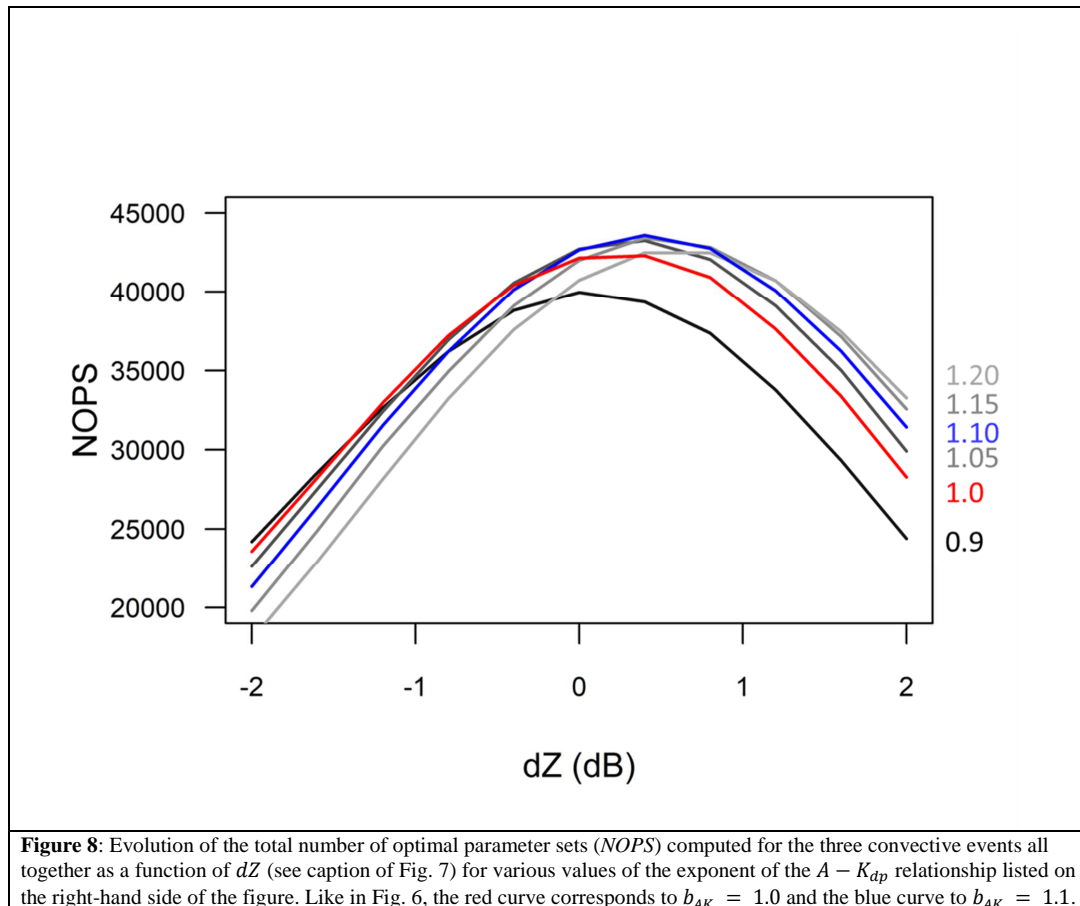
810





820





825

